communications materials

Article

https://doi.org/10.1038/s43246-024-00709-8

Stratification of fluoride uptake among enamel crystals with age elucidated by atom probe tomography

Jack R. Grimm [1,2], Cameron Renteria [1,3], Semanti Mukhopadhyay[2], Arun Devaraj [2,6] ✉ & Dwayne D. Arola [1,4,5,6] ✉

Dental enamel is subjected to a lifetime of de- and re-mineralization cycles in the oral environment, the cumulative effects of which cause embrittlement with age. However, the understanding of atomic scale mechanisms of dental enamel aging is still at its infancy, particularly regarding where compositional differences occur in the hydroxyapatite nanocrystals and what underlying mechanisms might be responsible. Here, we use atom probe tomography to compare enamel from a young (22 years old) and a senior (56 years old) adult donor tooth. Findings reveal that the concentration of fluorine is elevated in the shells of senior nanocrystals relative to young, with less significant differences between the cores or intergranular phases. It is proposed that the embrittlement of enamel is driven, at least in part, by the infusion of fluorine into the nanocrystals and that the principal mechanism is de- and re-mineralization cycles that preferentially erode and rebuild the nanocrystals shells.

Due to the diphyodont nature of humans and the acellular nature of enamel, an increasing life expectancy subjects the permanent dentition to more physical (i.e., cyclic contact) and chemical (i.e., demineralization) damage. To this end, there is an expanding effort to develop therapeutic approaches that can counteract the effects of aging and preserve the function of natural enamel. Such treatments will necessarily interface with the hydroxyapatite (HA, $Ca_{10}(PO_4)_6(OH)_2$) nanocrystals that constitute the fundamental unit of enamel. However, there is limited atomic scale understanding of the morphological and chemical changes that the HA nanocrystals undergo with age. The present study applies atom probe tomography (APT) to compare the composition of HA nanocrystals and the surrounding intergranular amorphous phase from young (<35 years of age) and senior (>55 years of age) adult human molar enamel.

Enamel, like many other mineralized tissues, has a complex hierarchical microstructure[1,2]. Optical microscopy on a polished cross section of enamel reveals light and dark bands approximately 50 μm wide (Fig. 1a), which correspond to decussated assemblies of enamel rods with diameters of ~5 μm. The rods are in turn constituted of HA nanocrystals with a cross section of ~50 × ~120 nm and many times longer in length[3–5]. The nanocrystal interfaces consist of several nanometers of amorphous mineral and organic residues[4,6–8]. Though small in size, even the HA nanocrystals appear to have been optimized through natural selection to improve the durability of enamel. For example, adjacent nanocrystals have distinct crystal lattice alignments, which increases the energy required for an incident crack tip to proceed from one nanocrystal to the next[9]. There is also evidence that compositional gradients within a single nanocrystal result in a residual compressive strain on the surface that improves both the mechanical and chemical properties[4]. A key knowledge gap is the influence of changes to the nanoscale composition of these nanocrystals with aging towards enhancing or diminishing the performance and longevity of the enamel tissue.

Chronological aging is a universal process which induces detrimental changes to the properties and performance of enamel. Specifically, it becomes harder, stiffer, more brittle, and thus more prone to mechanical failure, particularly near the outer enamel surface[10–13]. A pathway by which these changes are realized is the ion exchange induced by extended exposure to a dynamic oral environment. Demineralization by dietary choices with low pH and biofilm activity is counteracted by salivary action and regular dental care to balance the pH and introduce e.g., calcium and phosphate ions to remineralize the tissue[14]. The intergranular phase between nanocrystals is a known channel for the introduction of ions into enamel[15–17], exposing the nanocrystal shell to etchants and remineralizing agents alike and rendering it a prime location where ion exchanges may accumulate with age. While

[1]Department of Materials Science and Engineering, University of Washington, Seattle, WA, USA. [2]Physical and Computational Sciences Directorate, Pacific Northwest National Laboratory, Richland, WA, USA. [3]Department of Oral Health Sciences, School of Dentistry, University of Washington, Seattle, WA, USA. [4]Department of Mechanical Engineering, University of Washington, Seattle, WA, USA. [5]Department of Restorative Dentistry, School of Dentistry, University of Washington, Seattle, WA, USA. [6]These authors jointly supervised this work: Arun Devaraj, Dwayne D. Arola. ✉e-mail: arun.devaraj@pnnl.gov; darola@uw.edu

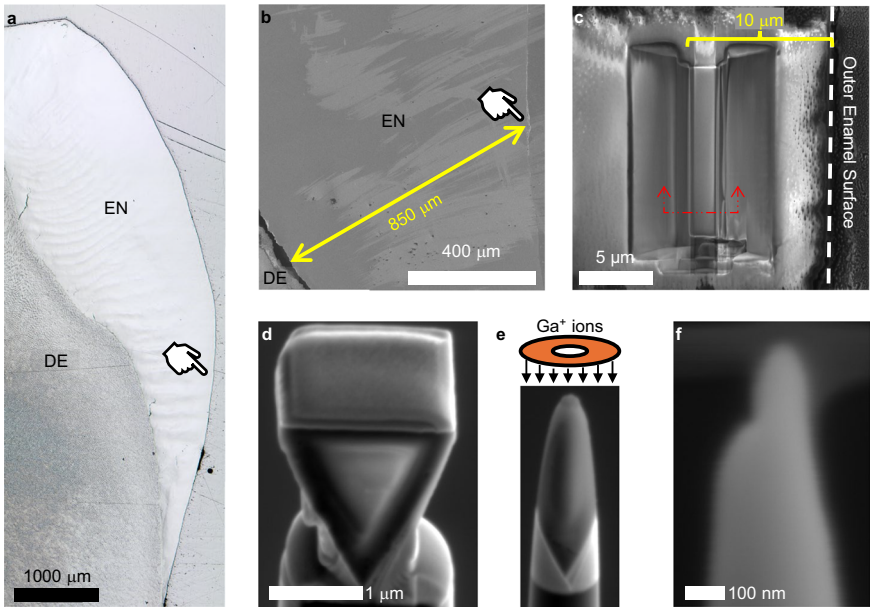

Fig. 1 | Preparation of samples for atom probe tomography. a Optical micrograph of polished cross section of young molar. **b** Scanning electron micrograph of cervical enamel from young molar, with enamel (EN) and dentin (DE) noted for clarity. The sample was taken from a location approximately 850 µm from the dentin-enamel junction, and (**c**) approximately 10 µm from the outer enamel surface. The cutting plane line indicates the sectional view of the cantilever presented in (**d**). **d** A cantilever with triangular cross section was produced in situ using focused ion beam milling to be lifted out. **e** A segment of the liftout was attached to a Si micropost then milled with progressively smaller annular ion beam patterns to shape the needle before a final low-kV polishing step was used to achieve a tip diameter <100 nm (**f**). The perspective of the micrographs in (**d**–**f**) is fixed and at a stage tilt of 52°, (**d**, **e**) are at the same scale.

there is no shortage of studies motivated to understand enamel dissolution by caries or dietary choices[16,18,19], how chronological aging in otherwise healthy enamel produces variations in the nanocrystal composition remains an open question.

There is no doubt that the composition is critically important, as evidenced by the well-known examples of fluoridated drinking water as a public service and fluoride-laden dental treatments to combat caries. Partially fluoridated apatite has a lower solubility than pure hydroxyapatite[20]. Excess fluoridation, however, is detrimental to the damage tolerant properties of enamel that are so critical to function, and in the extreme case, can be pathological (fluorosis)[21,22]. Various spectroscopy methods (e.g., energy dispersive, Raman, Fourier-transformed infrared) have been applied to enamel at the micron to millimeter scale to measure such compositional changes in bulk, e.g., Refs. 23–27. However, the introduction and exchange of ions will necessarily take place at the atomic level, presumably at curved nanoscale interfaces. Thus, in order to accurately observe compositional changes associated with age, 3D sub-nanometer scale resolution characterization techniques such as APT are needed.

In APT, a three-dimensional reconstruction of atom positions within a sample is achieved by subjecting a sharp needle to intense electric fields (10 s of V nm^{-1}) along with a femtosecond laser pulse to induce field evaporation of ions towards a two-dimensional detector[8,28]. The needle samples of non-conductive materials are often prepared by a focused ion beam liftout approach (Fig. 1c–f) that allows for precise site selection. Time-of-flight and hit location on the detector are recorded for each evaporated ion, which enables the physical position of each ion to be reconstructed with sub-nanometer resolution. The resultant reconstruction is then interrogated to discern nanoscale chemical gradients and features in materials.

APT has been used to reveal the distribution of elements and impurities in mature enamel[4,6,7,29,30]. In a study of murine incisors, Gordon et. al. showed that distinct HA nanocrystals can be identified by an amorphous calcium phosphate (ACP) intergranular phase, rich in Mg, organic residues, and other impurities[6,29]. This aligns with expectations from the post-classical theory of amelogenesis, wherein enamel maturation is thought to occur by transformation of ACP precursor nanoribbons into HA[31,32]. Mg initially serves to stabilize ACP, allowing the nanoribbons to grow in length before transforming to HA[25,31]. The HA crystal lattice has lower solubility for Mg[25]; as amelogenesis progresses and the nanocrystals transform and grow, Mg and residual organics are pushed to the intergranular spaces and concentrated there. Interestingly, in human molars, Mg is additionally enriched in the core of the nanocrystals[4], a notable departure from the prior studies of murine enamel[6]. The Mg segregation can thus be used to visually distinguish core, shell, and intergranular phases in enamel, enabling further analysis and comparison between phases in ex vivo samples.

To assess the nanoscale compositional modification that could potentially occur in human enamel with aging, we conducted APT analysis of the outer cervical enamel of young and senior adult molars. The APT results revealed that the concentration of fluorine was elevated in the shell regions of senior enamel nanocrystals relative to the young, providing evidence of the mechanism by which ion concentrations accumulate with age with 3D nanometer resolution.

Results

Atom probe tomography

Three APT datasets large enough to capture multiple HA nanocrystals (between 8.5×10^6—19×10^6 ions per dataset) were obtained for both the young (total = 37.2×10^6 ions) and senior enamel (total = 36.9×10^6 ions). Samples were collected within 10 µm of the outer enamel surface (OES) (Fig. 1a–c) as this region is most severely embrittled in senior enamel[10,13]. Enamel from the cervical portion of the tooth was utilized in this study as it is not directly subjected to the mechanical wear imposed by mastication, allowing for improved consistency between samples from different individuals or age groups.

The mass-to-charge spectra from each APT dataset exhibited on the order of 100 peaks, due to the complex field evaporation phenomena that take place. It is noted that the largest molecular ions primarily featured covalently bonded groups, from PO^+ at 46.969 Da to $P_4O_{10}+$ at 283.846 Da A segment of a representative spectra from 0 to 50 Da comparing the young and senior age groups and the chemical identity of each peak is presented in Fig. 2. The full version of the spectral comparison is presented in Supplementary Fig. 1. The most prominent peak in each spectra was the $^{40}Ca^{++}$ peak at 19.982 Da.

APT reconstruction of the enamel nanostructures (Fig. 3) shows that independent of age, Mg is segregated to the core of each nanocrystal as well as the intergranular space between them, which agrees with the findings of another recent study[4]. The core of each nanocrystal is visible as an ovular, nearly linear region with a relatively high density of Mg ions surrounded by a Mg-depleted shell. Between shell regions the Mg density increases again, forming a continuous intergranular phase separating each nanocrystal. The shell thickness is not uniform; the cores are not evenly centered, and in many

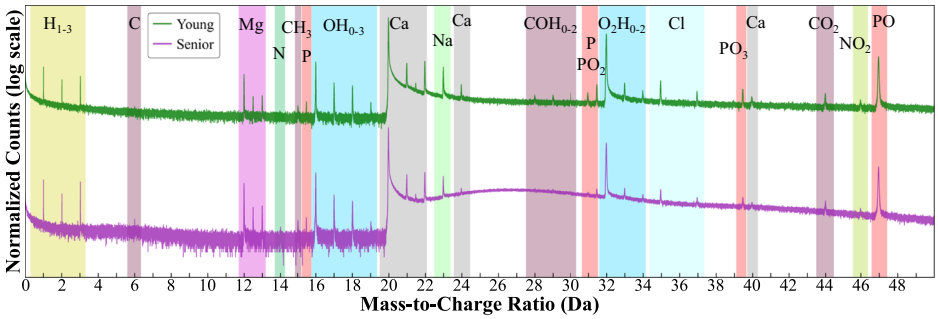

Fig. 2 | Labeled segment of representative mass-to charge spectra from young and senior enamel. A full list of the ranges used is provided in the supplementary information.

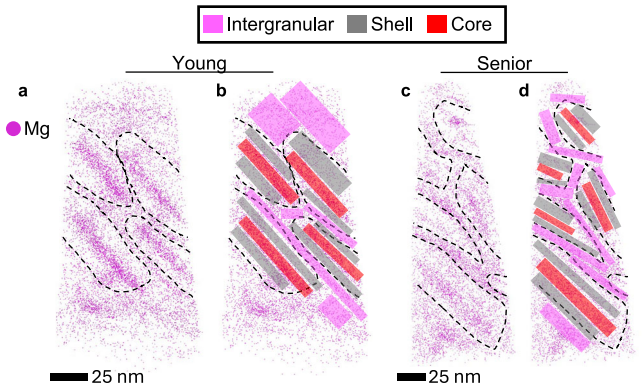

Fig. 3 | Representative APT reconstructions for young and senior enamel. Only the Mg ions are visible. **a**, **c** Properly aligned reconstructions show the Mg-enriched core of each nanocrystal surrounded by a Mg-depleted shell. The intergranular space between nanocrystals also has a relatively high Mg concentration. The boundaries of each nanocrystal are outlined. **b**, **d** Rectangular ROIs are drawn and assigned to the intergranular, shell, or core phase.

crystals, the core is observed to nearly contact the intergranular phase. The thickness of the intergranular phase is likewise nonuniform as some nanocrystals appear to almost impinge on each other while others are separated by tens of nm. As there is no definitive way to determine the edge of the nanocrystals based on ion concentrations, it is difficult to make a truly quantitative measure of the intergranular separation from APT alone. However, from approximate measures taken between the dashed lines in Fig. 3 and Supplementary Fig. 2, the average distance separating adjacent nanocrystals in the young enamel is ~3.9 nm, while that in the senior enamel is ~6.4 nm.

A two-tailed unequal variance *t*-test was performed to evaluate the strength of evidence for differences between the age groups, presented in Fig. 4 and Supplementary Data 3. There is moderate evidence that the senior enamel (0.136 ± 0.0064 at.% Mg, mean ± standard deviation) had a higher bulk concentration of Mg than the young (0.113 ± 0.0035 at.% Mg) enamel ($p = 0.019$), though there is no evidence of significant differences for any specific phase (Fig. 4b). However, there are highly significant differences in the F concentration. In particular, the shells of nanocrystals in senior enamel (0.113 ± 0.0066 at.% F) show significantly higher F relative to those in young enamel (0.096 ± 0.0049 at.% F, $p = 0.000595$). There is additionally strong evidence that the bulk concentration of F is higher in senior enamel ($p = 0.00263$). This trend also appears true for the intergranular and core phases, though the evidence is weaker ($p = 0.054$ and $p = 0.060$, respectively). In addition, the mean concentration of Na is higher in the young enamel for all phases, but there is no statistical evidence to support this trend (lowest $p = 0.117$ for bulk–bulk comparison, Fig. 4d). Interestingly, the concentration of C, including both organic and inorganic contributions, is almost identical between young and senior enamel for the bulk as well as each phase. The mean concentration of C in the intergranular phase of senior enamel appears slightly lower than that in the young enamel, but there is no evidence to support this difference ($p = 0.659$, Fig. 4e). Additional comparisons of N, Cl, CO, and CO_2 are provided in Supplementary Note 1 and Supplementary Fig. 4.

Scanning transmission electron microscopy

Scanning transmission electron microscopy (STEM) was used to compare the relative morphology and nanocrystal size between the young and senior enamel samples by extracting cross sections from locations near where the APT samples were taken. Representative high-angle annular dark field (HAADF)-STEM micrographs were obtained at high camera length to reveal locations of higher strain, as presented in Fig. 5. Nanocrystals with the expected elongated hexagonal cross section morphology and a core with darker contrast are readily seen in both samples. In the senior sample (Fig. 5b), the nanocrystal boundaries generally have good contrast, and the nanocrystals themselves are relatively well aligned and closely packed, though there are some gaps between misaligned nanocrystals. Nanocrystals that have a substantially brighter contrast may indicate higher lattice strain within these crystals. These bright crystals were observed far more frequently in the FIB lamella prepared from the senior enamel (Supplementary Fig. 5). In comparison, nanocrystals in the young enamel sample are not as closely packed, with gaps being somewhat larger and more frequent. Additionally, there are mineralized regions that do not conform to the expected morphology, appearing more equiaxed, globular, or fragmented. Several such regions are highlighted by arrows in Fig. 5a.

Dimensional comparisons reveal that the average nanocrystal dimensions (in cross sectional area, and major and minor axis lengths) are smaller for the senior enamel sample relative to the young (Fig. 5c–e and Supplementary Data 4). The nanocrystal cross sectional area is significantly different ($p = 5.3e{-}6$, unequal variances *t*-test) between the young (mean ± std = 3214 ± 1256 nm^2, $n = 38$) and senior (1993 ± 853 nm^2, $n = 38$) enamel samples. Similarly, the minor axis length of a fit ellipse drawn around each measured nanocrystal is significantly different ($p = 4.6e{-}6$, young = 38 ± 8 nm, senior = 30 ± 6 nm). There is also a difference in the long axis dimension between nanocrystals in the young (106 ± 28 nm) and senior (85 ± 30 nm) samples, though it is not as statistically significant ($p = 0.0015$).

Discussion

The mass-to-charge spectra were primarily dominated by Ca, O, and P-containing species. Smaller concentrations of impurity elements, such as Cl, Na, F, Mg, and C were also observed. In laser-pulsed APT of materials with low thermal conductivity, residual thermal energy from the laser pulse can cause mistimed evaporation events, which present as a thermal tail after prominent peaks. The senior enamel appears to have higher thermal tails after the Ca and O_2 peaks relative to the young samples (Fig. 2). This may suggest that the senior enamel has physical features such as cracks or porosity that hinder thermal dissipation. The presence of bright nanocrystals in the senior enamel of our STEM analyzes (Fig. 5b and Supplementary Fig. 5) may reflect nanocrystals with lattice strain that could impede thermal diffusivity. However, this is speculative and should be corroborated by

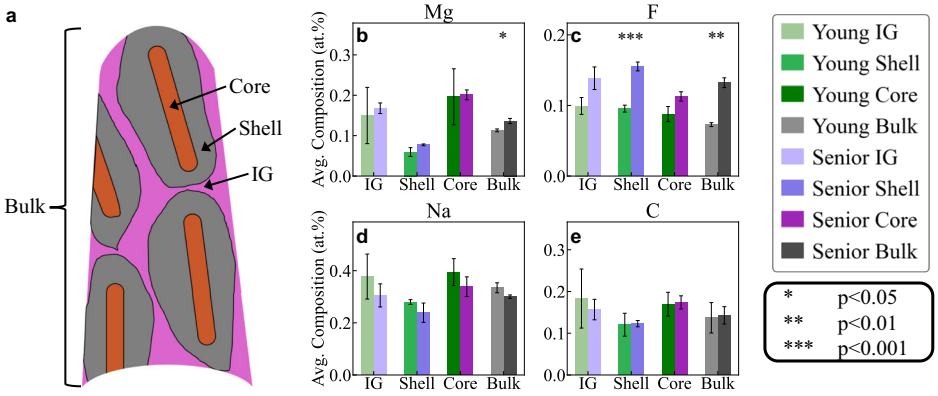

Fig. 4 | Comparison of minor element concentrations by nanocrystal phase. a Schematic of an APT reconstruction that has captured several hydroxyapatite nanocrystals, with phases labeled. **b**–**e** Average composition in atomic% of Mg, F, Na, and C, respectively. For each phase, data from the young sample is on the left, senior is on the right. Error bars represent one standard deviation, each dataset is represented as a point. These concentrations are measured after molecular ions (e.g., CaF) have been decomposed into their constituent elements.

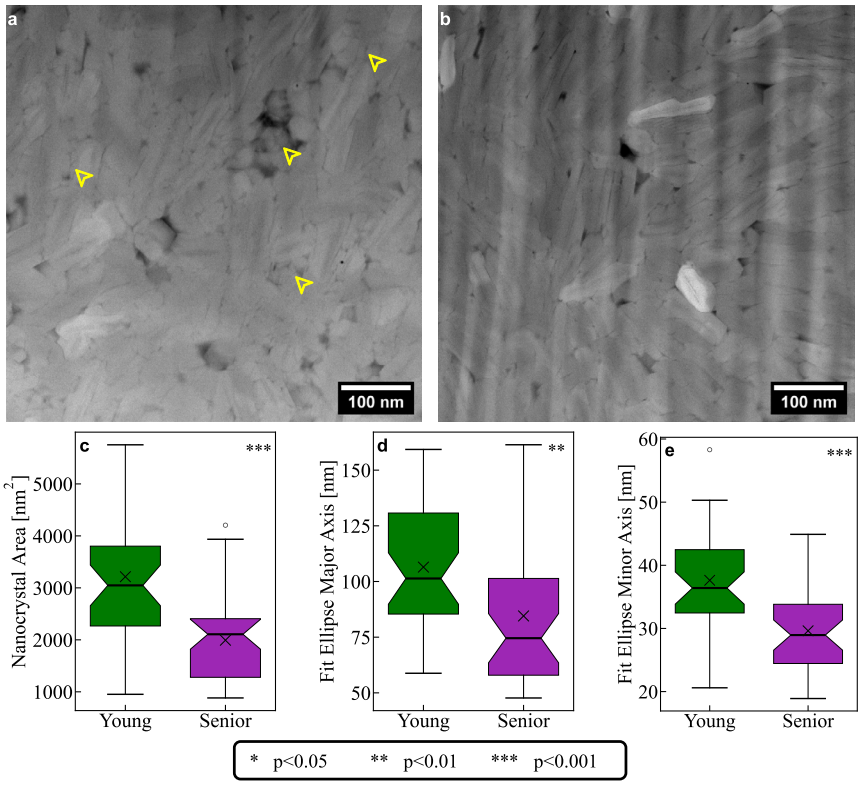

Fig. 5 | Comparison of nanocrystal dimensions and morphology by STEM high-angle annular dark field (HAADF). a Young enamel. The yellow pointers highlight several regions where the mineral domain appears equiaxed, globular, or fragmented. **b** Senior enamel. **c**–**e** Box-and-whisker plots summarizing the distribution of (**c**) nanocrystal area, (**d**) fit ellipse major axis length, and (**e**) fit ellipse minor axis length for individual nanocrystals measured by STEM. Asterisks in the upper right corner denote the *p* value from an unequal variance *t*-test. In each plot, the box encloses the second and third quartile, the line represents the median, the notch is the 95% confidence interval for the median, the *x* marks the mean, and the whiskers stretch beyond the box by 1.5 times the inter-quartile range. Outliers are marked by a hollow circle.

measurements of thermal conductivity from other techniques (e.g., scanning thermal microscopy [33] or infrared measurements[34]) before making any firm conclusions.

The nanocrystal shape, as outlined by the intergranular regions enriched in Mg (Fig. 3), agreed well with expectations from previous reports on enamel from APT, transmission electron microscopy, and atomic force microscopy in the literature[3–6,29,30,35]. It also agrees well with our own STEM analyses on these samples. Furthermore, the Mg-enriched core that has been previously reported in human enamel nanocrystals (Ref. 4) was observed here as well. These regions of Mg enrichment served as the basis by which ROIs belonging to the core, shell, and intergranular phases were assigned. While it is challenging to measure the borders of the nanocrystals with certainty from APT data alone, using the dashed outlines as in Fig. 3a, c, the intergranular thickness between nanocrystals is lower in the young samples. Measurements from STEM present a complimentary observation: the nanocrystals in young enamel are significantly larger (Fig. 5), which has also been observed by atomic force microscopy [35]. A size decrease of HA nanocrystals in dentin tubules with increasing age has also been reported[36,37]. Assuming that the number density of nanocrystals does not change with age, it follows that some volume of the nanocrystal shell is replaced by the intergranular phase over time. Such a pathway may also be responsible for the absence of the small mineral domains noted in the young enamel sample (Fig. 5a yellow pointers) in the senior enamel, but more dedicated study is required.

A probable mechanism for the higher F content in the nanocrystal shells of senior enamel relative to young (Fig. 4c) is the introduction and diffusion of F through the intergranular phase during the de- and remineralization cycles. When the enamel surface is exposed to an acid, it permeates through the intergranular spaces and reduces the diameter of the nanocrystals[16]. In the same vein, treatment with NaF solution results in strong segregation of both Na and F concentrations to the intergranular phase[4]. The outer enamel is exposed to both acidic and remineralizing agents cyclically on a daily basis, and it is during these remineralization cycles that F ions can be incorporated into the HA lattice structure[3,38].

Additionally, F substitutions within the HA lattice may diffuse further into the shell towards the core over time. Within the crystal structure of (hydroxy-, fluor- or chlor-) apatite, the interchangeable ion (OH^-, F^-, Cl^-) positions lie in a column along the vertical sixfold screw *c*-axis[39]. The columnar alignment of the lattice points eligible for substitution makes the c-axis the fastest channel for ion diffusion. It has been conventional knowledge that the hexagonal crystal structure is aligned with the approximately hexagonal nanocrystal morphology[5], but there is recent evidence that the crystal directions of two adjacent nanocrystals can be misaligned by several 10 s of degrees, even though the nanocrystals themselves appear well aligned[9]. This implies that the relatively fast-diffusing *c*-axis can be exposed to the intergranular phase, thereby enabling ion diffusion somewhat further into the nanocrystal.

The APT reconstructions showed only weak statistical evidence that the F concentrations of the intergranular and core phases were different between age groups (Fig. 4c). Because the intergranular phase is the channel by which acids and remineralizing agents permeate the enamel, it is in a state of constant flux and long-term changes are unable to accumulate. Conversely, because the core is not directly exposed to the intergranular phase, it is unlikely to be directly affected by de- and re-mineralization cycles. The F concentration gradient between shell and core provides a driving force for diffusion. However, F^- substitutions in a HA lattice interact with the neighboring OH^- groups through hydrogen bonds, which can limit the rate of diffusion, even along the *c*-axis[40]. Thus, the composition of the core is relatively stable over time.

The fluoride concentration is of considerable importance because it enhances the dissolution resistance of the mineral. Partially fluoridated HA has substantially lower solubility relative to pure hydroxyapatite, with minimum solubility at ~2.4 at.% F[20]. This is an order of magnitude larger than the F concentration observed via APT. However, the gradient of F concentration against distance from the enamel surface is very sharp, even within just the first 5 μm[41], so the nanocrystals surveyed here are expected to have less F than those at the immediate surface. It has also been shown that the difference in F concentration between young and senior enamel is more pronounced near the outer enamel surface[42]. Hence, a repeat of this study performed with tissue obtained closer to the enamel surface (perhaps even directly on the surface) would be expected to show similar trends, but with even greater difference between young and senior enamel.

Residual organic content between nanocrystals is a key component of crack growth resistance in enamel[43]. We hypothesize that residual organic content is leached out over time and replaced by mineral, contributing to the increase in brittleness, but there are challenges to assessing this with APT. From this data, a reliable method for determining whether a carbon-containing molecular ion is of organic (proteins and protein cleavage products) or inorganic (CO_3 substitutions in the HA lattice) origin could not be established. Additionally, none of the datasets collected for this study exhibited the organic- and Mg-rich precipitates that other groups have reported in enamel[7,30]. This is expected to be partly due to taking samples near the outer surface, where protein content is lowest[10,13,44]. It has been proposed that the CO^+ signal at 28 Da is associated with both organics and inorganics while CO_2^+ at 44 Da is only associated with inorganics based on their segregation within or outside of organic precipitates[7,45]. As shown in Supplementary Fig. 4, there was little to no statistical evidence in this case that the concentration of CO or CO_2 showed any trend with age between the young and senior enamel (Supplementary Fig. 4c, d). The same is true for N (Supplementary Fig. 4a), which would be expected to be associated with organics. A systematic study is underway to identify a reliable signature that can be used to investigate organic components in fully mineralized (i.e., no organic precipitates) regions of enamel using APT.

Admittedly, a higher F concentration in the outer enamel of seniors could be expected[10,11,42]. However, the spatial evaluations of F across individual crystal domains between individuals enabled by recent advances in APT provides a new perspective of the mechanisms at play. It is proposed that the intergranular amorphous mineral phase that separates the hydroxyapatite nanocrystals is the primary channel by which the de- and re-mineralization cycles of enamel occur. Fluorine (from e.g., fluoridated drinking water and other F-enriched dental products) is incorporated into the shells of nanocrystals during remineralization. While some diffusion of F ions through the nanocrystal surely occurs, the accumulation of F is largely restricted to the nanocrystal shell, suggesting that ion replacement during remineralization is the dominant mechanism.

There are recognized limitations to the present study that are important to consider. The primary limitation is the relatively small number of samples. Only one donor tooth from each age group was considered, and only three datasets were collected for each tooth. A small sample size cannot account for intrinsic variation between individuals owing to their lifestyle, diet, upbringing (i.e., exposure to fluoridated water in adolescence during permanent molar formation), or genetic predisposition. These are equally interesting topics that merit future evaluation. Nevertheless, we believe that the proposed model is a likely mechanism for the increased fluoride concentration in seniors that has been observed for some time with larger datasets[10,42]. Topical treatment by NaF (250 mM, pH 8.4, 37 °C, 24 h) shows that the captured F from exposure at this time scale is restricted to the intergranular phase[4]. Our interpretation of this is that the fluoride is unable to significantly diffuse and incorporate into the nanocrystal shells by direct exposure only. Here, we did not see a strong difference in the fluoride concentration in the intergranular space; it is unlikely that this is what drives the elevated F content in seniors. That leaves incorporation during de-/re-mineralization cycles as a likely mechanism by which F can accumulate over time.

One could question the clinical relevance of the research. We envision that the findings could help guide the development of clinical approaches to improve the efficacy of fluoride treatments in tooth protection. Key would be understanding the placement and degree of accumulation of fluorine within crystals. Clearly, APT could serve as a valuable resource in this effort. With regards to the accumulation of fluorine with age, the findings establish one aspect of change in crystallography that could be responsible for the increased hardness and embrittlement of enamel in older patients[10,46,47]. Modulating tooth protection and age-related embrittlement simultaneously has the potential for substantial clinical impact and the status of lifelong oral health.

Regrettably, APT is not easily applied to large sample sizes because access to the required instrumentation is costly, and it is time-intensive from sample preparation through data collection and analysis. However, the statistical methods employed herein identified highly significant differences in composition and can be readily applied to larger datasets as automation capabilities for both data collection and analysis continue to improve. Furthermore, although this study was focused primarily on fluorine, there are other components, including carbonate substitutions, organic residues, and nanocrystal morphology, that undoubtedly contribute to the degradation in mechanical properties of senior enamel as well, and warrant further investigation. The findings emphasize that compositional modifications as a result of aging accumulate with the chronological clock. Key to mitigating the age-induced degradation of enamel will be identifying those nanoscale factors that accelerate the aging process, the underlying mechanisms, and the most appropriate avenues for therapeutic treatment.

Methods

Anonymous human third molars were obtained for this investigation from the Dental School at the University of Washington in Seattle, WA, under an IRB exemption for STUDY00014724 from the University of Washington institutional review board. The young and senior third molars were free of fillings or carious lesions and were obtained from a 22 year old and a 56 year old donor, respectively. Upon receipt, the teeth and tissue waste were sterilized using a freshly prepared 1:10 dilution of 0.5% sodium hypochlorite. The teeth were sectioned buccal-lingually along the midline of the tooth using a wire saw (STX-202A, MTI Corporation) with copious water as coolant. Each tooth was allowed to dry at room conditions, then one half was stored while the other was mounted in a two-part epoxy (EpoFix resin and hardener, Struers). The mounted sections were ground with a sequence of

SiC papers (ISO numbers 800, 1200, 2400, 4000), ultrasonicated, and polished with diamond suspensions (particle sizes 3, 0.5 µm; Struers) on separate polishing cloths (MD-Dac, Struers). Polished samples were stored in a desiccator for at least 48 h to release unbound water, then sputter coated with 10 nm of Pt for conductivity (ACE600, Leica).

Samples were prepared for APT using a typical liftout procedure in a dual-beam focused ion beam scanning electron microscope (FIB-SEM; Helios and/or Quanta, both manufactured by Thermo Fisher Scientific). A protective Pt coating was deposited on a region of interest that was ~10 µm from the OES and ~850 µm from the dentin-enamel junction (DEJ). Trenches were then milled on either side and one edge of the coated strip at a 30° incidence angle using a 30 kV 1 nA ion beam and cleaned of redeposited material with a second pass. The cantilever was attached to a nanomanipulator (Omniprobe) by a Pt weld then freed from the bulk material with a thin ion beam cut. The liftout was attached to a coupon of prepared Si microposts designed for APT (M22 array, Cameca) with Pt welds. To produce a sharp needle for APT, each sample was polished using annular ion beam milling. Final polishing of the needle was completed at 5 kV to remove the Ga-implanted region (~30–200 nm of enamel). Full details are provided in the Supplementary Methods.

Experiments were run in a local electrode atom probe (LEAP 4000 XHR, Cameca) in laser pulsing mode with a pulse energy of 60 pJ, a pulse frequency of 125 kHz, a base temperature of 40 K, and a target detection rate of 0.5%. This resulted in a charge state ratio for Ca^{++}/Ca^{+} of ~1400.

Reconstructions of the APT data were performed using the integrated visualization and analysis software (IVAS version 3.8.10, Cameca). Ranges were drawn to include those portions of the peak that had a signal with twice as many counts as the surrounding background. A full list of the ranges used is provided in Supplementary Data 1. Voltage-based tip evolution was used to drive the reconstruction, assigning Ca with a field evaporation of 18 V nm^{-1} as the primary element, with default element specific atomic volumes, a detector efficiency of 0.36, k factor of 3.30, and an image compression factor of 1.650.

Regions of interest (ROIs) were generated by first rotating the reconstruction with only Mg ions visualized until the displayed ions aligned and the core-shell structures and intergranular areas became clear (see Supplementary Movie 1). The approximate boundaries of each nanocrystal were traced (see Fig. 3a,c and Supplementary Fig. 2a, c, e, g), and then segmented with rectangular ROIs drawn on each phase (Fig. 3b, d and Supplementary Fig. 2b, d, f, h). The size of the ROIs associated with the intergranular and core phases was adjusted to encapsulate the region of highest Mg concentration, whereas those associated with shell phase were sized to fill the spaces between core and intergranular ROIs. An effort was made to encapsulate as much of the reconstruction as possible, but without any overlapping of adjacent ROIs. Additionally, as the length of HA nanocrystals in enamel is many times longer than their cross section, each nanocrystal observed in the APT dataset was assumed to extend well beyond the reconstructed volume, and so the ROIs extend through the whole width of the reconstruction (into/out of the page in Fig. 3b, d and Supplementary Fig. 2b, d, f, h).

A frequency distribution analysis with 10-ion blocks was exported from each ROI as.csv files then loaded into a custom python (version 3.11) script for analysis. The background-subtracted mass-to-charge spectra from each ROI (10 s of ROIs per dataset) were ranged using the same.rrng file as the overall reconstruction they belong too, then the count of each ranged ion summed in a custom jupyter notebook by phase (3 phases per dataset). This condensed the composition of each dataset into just three compositions, one for each phase, rather than one for each ROI. The statistical strength of comparisons between the three phases and the two age groups were evaluated using the scipy package for one-way ANOVA (scipy.stats.anova) and unequal variance *t*-test (`scipy.stats.t`), respectively and results are presented in Supplementary Data 2.

To add a measure of statistical confidence that the ROIs were drawn and labeled appropriately, the Mg concentration was assessed by both histogram and frequency distribution analysis. For both age groups, core ROIs tended to have the highest Mg concentration compared to the shell ROIs with the lowest, while intergranular ROIs fell in intermediate ranges (Supplementary Fig. 3a). Using a frequency distribution analysis to compare the similarity of each pair of ROIs showed that same-phase pairs (e.g., core ROI vs. core ROI) were more similar than different-phase pairs (e.g., core ROI vs. shell ROI, Supplementary Fig. 3b). These methods and their findings are discussed in greater detail in the Supplementary Discussion; both methods supported the assignment of ROIs into three distinct phases.

Samples for scanning transmission electron microscopy (STEM) were prepared using a plasma FIB (Hydra, Thermo Fisher) using a typical liftout approach, full details can be found in the Supplementary information. Briefly, a protective Pt cap was first deposited over the region of interest, which was then milled using the Xe ion beam and attached to a nanomanipulator (EZLift, Thermo Fisher). Foils were attached to a 5-post Cu TEM Grid (Ted Pella) and thinned to a thickness of approximately 100 nm using a rocking polish technique. Additional details of sample preparation are provided in the Supplementary Methods. The foils were extracted from the same teeth used for the APT data collection at a location <50 µm from the site of the APT liftout and 10 µm from the OES.

STEM was performed on a ThermoFischer Scientific Themis Z 30–300 kV monochromated aberration corrected S/TEM, operated at 300 kV with spot size of 9. Imaging was performed with a 70 µm probe forming aperture, 29 pA screen current, and camera length of 185 mm.

Nanocrystal size measurement was conducted in ImageJ version 1.54 g (National Institutes of Health, USA). After setting the scale of the image, the freehand tool was used to outline individual nanocrystals from STEM micrographs collected at 165,000 × magnification. Only nanocrystals for which the edges could be clearly defined were measured. The area of the enclosed nanocrystal as well as the major and minor axes of the fit ellipse around the drawn shape were recorded. An unequal variance *t*-test (scipy.stats.t in python v3.11) was used to evaluate significance of comparisons.

Data availability

All data used to support the findings of this study are available in the main text or the supplementary materials and data files. The raw APT data,.rrng files, and reconstructions, as well as the TEM micrographs used in this study are available on the Zenodo repository at https://doi.org/10.5281/zenodo.11111719.

Received: 26 June 2024; Accepted: 30 November 2024;
Published online: 19 December 2024

References

1. Bajaj, D. & Arola, D. D. On the R-curve behavior of human tooth enamel. *Biomaterials* **30**, 4037–4046 (2009).
2. Yilmaz, E. D., Schneider, G. A. & Swain, M. V. Influence of structural hierarchy on the fracture behaviour of tooth enamel. *Philos. Trans. R. Soc. Math. Phys. Eng. Sci.* **373**, 20140130 (2015).
3. Yanagisawa, T. & Miake, Y. High-resolution electron microscopy of enamel-crystal demineralization and remineralization in carious lesions. *J. Electron Microsc.* **52**, 605–613 (2003).
4. DeRocher, K. A. et al. Chemical gradients in human enamel crystallites. *Nature* **583**, 66–71 (2020).
5. Kerebel, B., Daculsi, G. & Kerebel, L. M. Ultrastructural studies of enamel crystallites. *J. Dent. Res.* **58**, 844–851 (1979).
6. Gordon, L. M. et al. Amorphous intergranular phases control the properties of rodent tooth enamel. *Science* **347**, 746–750 (2015).
7. Fontaine, A. L. et al. Atomic-scale compositional mapping reveals Mg-rich amorphous calcium phosphate in human dental enamel. *Sci. Adv.* **2**, e1601145 (2016).
8. Grandfield, K. et al. Atom probe tomography for biomaterials and biomineralization. *Acta Biomater.* **148**, 44–60 (2022).
9. Beniash, E. et al. The hidden structure of human enamel. *Nat. Commun.* **10**, 4383 (2019).

10. Renteria, C., Yan, W., Huang, Y. L. & Arola, D. D. Contributions to enamel durability with aging: an application of data science tools. *J. Mech. Behav. Biomed.* **129**, 105147 (2022).
11. Yan, W., Renteria, C., Huang, Y. & Arola, D. D. A machine learning approach to investigate the materials science of enamel aging. *Dent. Mater.* **37**, 1761–1771 (2021).
12. He, B. et al. Mineral densities and elemental content in different layers of healthy human enamel with varying teeth age. *Arch. Oral. Biol.* **56**, 997–1004 (2011).
13. Park, S., Wang, D. H., Zhang, D., Romberg, E. & Arola, D. Mechanical properties of human enamel as a function of age and location in the tooth. *J. Mater. Sci. Mater. Med.* **19**, 2317–2324 (2008).
14. Buzalaf, M. A. R., Hannas, A. R. & Kato, M. T. Saliva and dental erosion. *J. Appl. Oral. Sci.* **20**, 493–502 (2012).
15. Kruzic, J. J., Hoffman, M. & Arsecularatne, J. A. Fatigue and wear of human tooth enamel: a review. *J. Mech. Behav. Biomed.* **138**, 105574 (2022).
16. Xiao, H., Arsecularatne, J. A., Zheng, J., Hoffman, M. J. & Zhou, Z. Effect of HAP crystallite orientation upon corrosion and tribocorrosion behavior of bovine and human dental enamel. *Corros. Sci.* **190**, 109670 (2021).
17. Hemingway, C. A., Parker, D. M., Addy, M. & Barbour, M. E. Erosion of enamel by non-carbonated soft drinks with and without toothbrushing abrasion. *Br. Dent. J.* **201**, 447–450 (2006).
18. Free, R., DeRocher, K., Xu, R., Joester, D. & Stock, S. R. A method for mapping submicron-scale crystallographic order/disorder applied to human tooth enamel. *Powder Diffr.* **35**, 117–123 (2020).
19. Arafa, A., Filfilan, S. S. & Fansa, H. A. Erosive effect of beverages on surface hardness and ultra-structure of deciduous teeth enamel. *Pediatr. Dent. J.* **32**, 186–192 (2022).
20. Moreno, E. C., Kresak, M. & Zahradnik, R. T. Fluoridated hydroxyapatite solubility and caries formation. *Nature* **247**, 64–65 (1974).
21. Min, J. et al. Investigation on the gradient nanomechanical behavior of dental fluorosis enamel. *Nanoscale Res. Lett.* **13**, 347 (2018).
22. Houari, S. et al. Multi-scale characterization of developmental defects of enamel and their clinical significance for diagnosis and treatment. *Acta Biomater.* **169**, 155–167 (2023).
23. Sa, Y. et al. Compositional, structural and mechanical comparisons of normal enamel and hypomaturation enamel. *Acta Biomater.* **10**, 5169–5177 (2014).
24. Xu, C., Reed, R., Gorski, J. P., Wang, Y. & Walker, M. P. The distribution of carbonate in enamel and its correlation with structure and mechanical properties. *J. Mater. Sci.* **47**, 8035–8043 (2012).
25. Legfros, R. Z., Sakae, T., Bautista, C., Retino, M. & Legeros, J. P. Magnesium and carbonate in enamel and synthetic apatites. *Adv. Dent. Res.* **10**, 225–231 (1996).
26. de Lopes, C. C. A., Limirio, P. H. J. O., Novais, V. R. & Dechichi, P. Fourier transform infrared spectroscopy (FTIR) application chemical characterization of enamel, dentin and bone. *Appl. Spectrosc. Rev.* **53**, 747–769 (2018).
27. Chen, J. et al. Effects of fluorine on the structure of fluorohydroxyapatite: a study by XRD, solid-state NMR and Raman spectroscopy. *J. Mater. Chem. B* **3**, 34–38 (2014).
28. Devaraj, A. et al. Three-dimensional nanoscale characterisation of materials by atom probe tomography. *Int. Mater. Rev.* **63**, 1–34 (2017).
29. Gordon, L. M. & Joester, D. Mapping residual organics and carbonate at grain boundaries and the amorphous interphase in mouse incisor enamel. *Front. Physiol.* **6**, 57 (2015).
30. Yun, F. et al. Nanoscale pathways for human tooth decay – central planar defect, organic-rich precipitate and high-angle grain boundary. *Biomaterials* **235**, 119748 (2020).
31. Simmer, J. P., Richardson, A. S., Hu, Y.-Y., Smith, C. E. & Hu, J. C.-C. A post-classical theory of enamel biomineralization… and why we need one. *Int. J. Oral. Sci.* **4**, 129–134 (2012).
32. Beniash, E., Metzler, R. A., Lam, R. S. K. & Gilbert, P. U. P. A. Transient amorphous calcium phosphate in forming enamel. *J. Struct. Biol.* **166**, 133–143 (2009).
33. Zhang, Y. et al. A review on principles and applications of scanning thermal microscopy (SThM). *Adv. Funct. Mater.* **30**, 1900892 (2020).
34. Lin, M. et al. A new method for characterization of thermal properties of human enamel and dentine: influence of microstructure. *Infrared Phys. Technol.* **53**, 457–463 (2010).
35. Leiva-Sabadini, C., Schuh, C. M., Barrera, N. P. & Aguayo, S. Ultrastructural characterisation of young and aged dental enamel by atomic force microscopy. *J. Microsc.* **288**, 185–192 (2022).
36. Porter, A. E. et al. A transmission electron microscopy study of mineralization in age-induced transparent dentin. *Biomaterials* **26**, 7650–7660 (2005).
37. Kinney, J. H., Nalla, R. K., Pople, J. A., Breunig, T. M. & Ritchie, R. O. Age-related transparent root dentin: mineral concentration, crystallite size, and mechanical properties. *Biomaterials* **26**, 3363–3376 (2005).
38. Miake, Y., Saeki, Y., Takahashi, M. & Yanagisawa, T. Remineralization effects of xylitol on demineralized enamel. *J. Electron Microsc.* **52**, 471–476 (2003).
39. Kay, M. I., Young, R. A. & Posner, A. S. Crystal structure of hydroxyapatite. *Nature* **204**, 1050–1052 (1964).
40. Young, R. A., der Lugt, W. V. & Elliott, J. C. Mechanism for fluorine inhibition of diffusion in hydroxyapatite. *Nature* **223**, 729–730 (1969).
41. Munksgaard, E. C. & Bruun, C. Determination of fluoride in superficial enamel biopsies from human teeth by means of gas chromatography. *Arch. Oral. Biol.* **18**, 735–743 (1973).
42. Isaac, S., Brudevold, F., Smith, F. A. & Gardner, D. E. The relation of fluoride in the drinking water to the distribution of fluoride in enamel. *J. Dent. Res.* **37**, 318–325 (1958).
43. Yahyazadehfar, M. & Arola, D. The role of organic proteins on the crack growth resistance of human enamel. *Acta Biomater.* **19**, 33–45 (2015).
44. Cuy, J. L., Mann, A. B., Livi, K. J., Teaford, M. F. & Weihs, T. P. Nanoindentation mapping of the mechanical properties of human molar tooth enamel. *Arch. Oral. Biol.* **47**, 281–291 (2002).
45. Taylor, S. D. et al. Resolving protein-mineral interfacial interactions during in vitro mineralization by atom probe tomography. *Mater. Today Adv.* **18**, 100378 (2023).
46. Park, S., Quinn, J. B., Romberg, E. & Arola, D. On the brittleness of enamel and selected dental materials. *Dent. Mater.* **24**, 1477–1485 (2008).
47. Yahyazadehfar, M., Zhang, D. & Arola, D. On the importance of aging to the crack growth resistance of human enamel. *Acta Biomater.* **32**, 264–274 (2016).

Acknowledgements

Colgate-Palmolive Company (D.A.). National Institutes of Health National Institute of Dental and Craniofacial Research grant DE-015347 (J.G., A.D.). National Institutes of Health National Institute of Dental and Craniofacial Research grant T90 DE-021984 (C.R.). Sample preparation with FIB and measurements with APT (Cameca LEAP 4000XHR) were performed at Pacific Northwest National Laboratory using facilities in the Environmental Molecular Sciences Laboratory, a DOE Office of Science User Facility sponsored by the Biological and Environmental Research program under Contract No. DE-AC05-76RL01830.

Author contributions

Conceptualization: D.A., J.G., and C.R. Data Curation: J.G. Formal Analysis: J.G. Methodology: J.G., C.R., S.M., and A.D. Investigation: J.G. and S.M. Visualization: J.G. Supervision: D.A. and A.D. Writing—original draft: J.G. Writing—review & editing: J.G., D.A., A.D., C.R., and S.M.

Competing interests

The authors declare no competing interests.

Additional information

Supplementary information The online version contains supplementary material available at https://doi.org/10.1038/s43246-024-00709-8.

Correspondence and requests for materials should be addressed to Arun Devaraj or Dwayne D. Arola.

Peer review information *Communications materials* thanks the anonymous reviewers for their contribution to the peer review of this work. Primary Handling Editors: Jet-Sing Lee.